Published in final edited form as:
Nano Res. 2017 April ; 10(4): 1366–1376. doi:10.1007/s12274-017-1472-z.

Targeting orthotopic gliomas with renal-clearable luminescent gold nanoparticles

Chuanqi Peng[1], **Xiaofei Gao**[2], **Jing Xu**[1], **Bujie Du**[1], **Xuhui Ning**[1], **Shaoheng Tang**[1], **Robert M. Bachoo**[3], **Mengxiao Yu**[1], **Woo-Ping Ge**[2], and **Jie Zheng**[1]

[1]Department of Chemistry and Biochemistry, The University of Texas at Dallas, Richardson, TX 75080, USA

[2]Children's Research Institute, Department of Pediatrics, Department of Neuroscience, Harold C. Simmons Comprehensive Cancer Center, UT Southwestern Medical Center, Dallas, TX 75390, USA

[3]Simmons Cancer Center, Annette G. Strauss Center for Neuro-Oncology, Department of Internal Medicine, Department of Neurology and Neurotherapeutics, UT Southwestern Medical Center, Dallas, TX 75390, USA

Abstract

A major clinical translational challenge in nanomedicine is the potential of toxicity associated with the uptake and long-term retention of non-degradable nanoparticles (NPs) in major organs. The development of inorganic NPs that undergo renal clearance could potentially resolve this significant biosafety concern. However, it remains unclear whether inorganic NPs that can be excreted by the kidneys remain capable of targeting tumors with poor permeability. Glioblastoma multiforme, the most malignant orthotopic brain tumor, presents a unique challenge for NP delivery because of the blood-brain barrier and robust blood-tumor barrier of reactive microglia and macroglia in the tumor microenvironment. Herein, we used an orthotopic murine glioma model to investigate the passive targeting of glutathione-coated gold nanoparticles (AuNPs) of 3 nm in diameter that undergo renal clearance and 18-nm AuNPs that fail to undergo renal clearance. Remarkably, we report that 3-nm AuNPs were able to target intracranial tumor tissues with higher efficiency (2.3× relative to surrounding non-tumor normal brain tissues) and greater specificity (3.0×) than did the larger AuNPs. Pharmacokinetics studies suggested that the higher glioma targeting ability of the 3-nm AuNPs may be attributed to the longer retention time in circulation. The total accumulation of the 3-nm AuNPs in major organs was significantly less (8.4×) than that of the 18-nm AuNPs. Microscopic imaging of blood vessels and renal-clearable AuNPs showed extravasation of NPs from the leaky blood-tumor barrier into the tumor interstitium. Taken together, our results suggest that the 3-nm AuNPs, characterized by enhanced permeability and retention, are able to target brain tumors and undergo renal clearance.

Correspondence to: Woo-Ping Ge; Jie Zheng.

Electronic Supplementary Material: Supplementary material (particle characterization and whole brain *ex vivo* imaging) is available in the online version of this article at http://dx.doi.org/10.1007/s12274-017-1472-z.

Keywords

enhanced permeability and retention; brain tumor; passive targeting; gold nanoparticles; renal clearance

1 Introduction

The enhanced permeability and retention (EPR) effect of nanoparticles (NPs), initially proposed by H. Maeda and co-workers three decades ago, has been the driving design principle for nanomedicines [1–4]. Tumor angiogenesis characterized by leaky, dilated microvasculature permits extravasation of NPs, while physical and physiological barriers, including poorly developed lymphatic systems within the tumor parenchyma, retard NP clearance [5–8]. As a result, NPs can selectively accumulate in tumors at high concentrations (10–50 folds higher than that in surrounding normal tissues within 1–2 days) [9]. However, targeting brain tumors through the systemic circulation is especially challenging. The endothelial tight junctions forming the blood-brain barrier with associated pericyte and astrocyte foot-process coverage represent a formidable physical barrier to NP delivery. These physiological structures effectively lower the cut-off pore sizes for gliomas (U87 MG, 7–100 nm), relative to the same tumors grown in the subcutaneous space (200–1,200 nm) [10–13]. The targeting efficiency of NPs in intracranial xenograft brain tumors (EPR < 0.1 %ID/g, percentage of injected dose per gram of tissue) [14–16] has been reported to be much lower compared to that in subcutaneous brain tumors (0.1–1 %ID/g) [17–24] and other non-central nervous system (CNS) tumors (1–10 %ID/g) [25–29].

To date, urinary excretion is believed to reduce the EPR effect of NPs because it might shorten their blood retention [30, 31]. On the other hand, non-specific accumulation of large inorganic NPs in the liver and spleen has severely limited the clinical utility of NPs because of potential health hazards deemed by regulations within the Food and Drug Administration [32–35]. While this biosafety concern could potentially be solved by developing NPs that are efficiently cleared by the renal route, it naturally raises a fundamental question of whether renal-clearable inorganic NPs still exhibit tumor-selective distribution and long retention via excretion. We recently reported that zwitterionic gold NPs (AuNPs, glutathione-coated) of 3 nm in diameter exhibited typical tumor-targeting behaviors with EPR similar to their larger non-renal-clearable counterparts [36]. The targeting efficiency of renal-clearable AuNPs could be further enhanced by increasing their circulation retention time [37]. Because of their ultrasmall sizes, it is critical to investigate whether renally cleared AuNPs would retain the ability to target orthotopic brain tumors, such as glioblastoma multiforme, that are known to have poor leakage [38].

Here, we report that renal-clearable zwitterionic glutathione-coated gold nanoparticles (GS-AuNPs) with a hydrodynamic diameter (HD) of 3 nm could passively target gliomas with higher efficiency (2.3 times) and specificity (3.0 times, defined as tumor-to-normal brain ratio) compared to non-renal-clearable 18-nm GS-AuNPs. Furthermore, both glioma targeting efficiency studies with inductively coupled plasma mass spectrometry and colocalization of fluorescence images of 3-nm renal-clearable AuNPs and tumor vessels suggested that nearly 56% of the AuNPs could escape leaky brain tumor vessels and enter the tumor microenvironment.

2 Results and discussion

2.1 Preparation of 3-nm and 18-nm zwitterionic AuNPs

The AuNPs to target brain tumors were designed in a spherical shape with the same zwitterionic surface (glutathione) but different sizes. The renal-clearable AuNPs were synthesized by thermal reduction of chloroauric acid ($HAuCl_4$) as reported previously [36]. The non-renal-clearable AuNPs were prepared by solid-state thermal reduction of gold salt with glycine [39] and surface replacement with zwitterionic glutathione ligands. The surface replacement was a rapid process where the thiol (–SH) group of glutathione could instantly form Au–S bonds with the 18-nm glycine-coated AuNPs (Gly-AuNPs). The unique absorbance of glutathione (UV range of ~200 nm) from the 18-nm AuNPs after replacement confirmed the effective surface glutathione coating compared with the 18-nm Gly-AuNPs from UV–Vis absorption measurements in Fig. S2 (in the Electronic Supplementary Material (ESM)). In addition, the 18-nm GS-AuNPs exhibited significantly increased surface charge compared with that of the 18-nm Gly-AuNPs: The zeta potential of the 18-nm GS-AuNPs was −42.8 ± 1.9 mV compared with that of −15.8 ± 1.6 mV for the 18-nm Gly-AuNPs (Fig. S3 in the ESM). The renal-clearable AuNPs were characterized with a core size of 2.6 ± 0.4 nm based on transmission electron microscopy measurements (Figs. 1(a) and 1(c)) and HD of 3.4 ± 0.4 nm obtained by dynamic light scattering (Fig. S1 in the ESM), consistent with a previous report [36]. Meanwhile, the non-renal-clearable AuNPs showed a core size of 17.4 ± 2.4 nm (Figs. 1(b) and 1(c)) and HD of 18.4 ± 3.2 nm (Fig. S1 in the ESM).

Because of the collective oscillation of free electrons in large AuNPs, the 18-nm AuNPs presented a characteristic plasmonic absorption peak at 524 nm (Fig. 1(d)), which was absent in the 3-nm AuNPs. Besides, the 3-nm AuNPs exhibited near-infrared (NIR) luminescent property with an emission peak at 810 nm under excitation at 350 nm (Fig. 1(e)), which allowed the *in vivo*, *ex vivo*, and fluorescence microscopy imaging of glioma targeting via the NPs.

2.2 Comparison of 3-nm and 18-nm AuNPs in glioma targeting, body clearance, and biodistribution

To conduct glioma targeting studies, 73c murine glioma cells ($p53^{-/-}Pten^{-/-}Braf^{V600E}$) [40] were implanted and gliomas were developed intracranially in the left hemisphere of mice. The 73c cells are very aggressive glioma cells, and gliomas (2–4 mm in diameter) formed within two weeks in mice transplanted with 10^4 cells. The glioma-bearing mice were intravenously injected with 3-nm or 18-nm AuNPs. At 24 h post-injection (p.i.), the mice were anesthetized and perfusion was performed to remove the AuNPs in the bloodstream before the mice were euthanized. Then the gliomas as well as normal brain tissues (brain region with no gliomas) were collected, and gold concentrations were analyzed with inductively coupled plasma mass spectrometry (ICP-MS).

The two AuNPs showed distinct differences in passive glioma targeting as shown in Fig. 2(a). The 3-nm AuNPs managed to accumulate specifically in the glioma through the EPR effect with a targeting efficiency of 0.18 ± 0.04 %ID/g, which was 2.3 times higher than that of the 18-nm AuNPs (0.08 ± 0.05 %ID/g). This was also higher than the passive targeting efficiencies of many other non-renal-clearable NPs, for instance, inorganic (iron oxide) nanoparticles (0.07 %ID/g) [15] and polymeric dendrimers with PEGylated modification (0.14 %ID/g) [14]. Additionally, both 3-nm and 18-nm AuNPs showed very low and comparable accumulation in normal brain (0.015 versus 0.019 %ID/g, respectively) because of the tight blood-brain barrier junction. As a result, the glioma targeting specificity (defined as tumor-to-normal brain ratio) of the 3-nm AuNPs was about 12.0, which was three times higher than that of the 18-nm AuNPs.

The higher targeting efficiency and specificity of the 3-nm AuNPs were mainly attributed to their long retention in blood. From pharmacokinetics study, the 3-nm AuNPs had a longer distribution half-life ($T_{1/2\alpha}$ = 0.73 h) and elimination half-life ($T_{1/2\beta}$ = 8.09 h) than those of the 18-nm AuNPs ($T_{1/2\alpha}$ = 0.08 h and $T_{1/2\beta}$ = 3.81 h) (Fig. 2(b)). The area under curve (AUC) of pharmacokinetics for the 3-nm AuNPs (34.2 %ID·h/g) was 2.1 times higher than that of the 18-nm AuNPs (16.2 %ID·h/g), facilitating the extravasation of renal-clearable AuNPs from leaky cancerous blood vessels.

Quantitative analysis of renal clearance and the biodistribution of nanoparticles also revealed the disparity in excretion routes between the AuNPs with sizes below and above the kidney filtration threshold (KFT). Because of the small HD below the KFT and resistance to serum protein adsorption, the 3-nm AuNPs were excreted into urine with an efficiency of 52.5 %ID within 24 h (Fig. 2(c)), which was known as a characteristic feature of renal-clearable AuNPs. In contrast, renal clearance of the 18-nm AuNPs was negligible; only 1.6 %ID was detected from urine at 24 h p.i.

Efficient renal clearance of the 3-nm AuNPs rendered their lower non-specific distribution in major organs than that of non-renal-clearable 18-nm AuNPs. The small 3-nm AuNPs showed fairly low distribution in normal organs (heart, liver, spleen, and lungs, <3 %ID/g) and tissues (skin and muscle, <1 %ID/g) at 24 h p.i., as shown in Fig. 2(d), whereas the 18-nm AuNPs ended up with massive accumulation at around 70.7 %ID/g in the liver and 25.0 %ID/g in the spleen. As a result, the overall distribution of the 18-nm AuNPs in major organs (heart, lungs, liver, spleen, and kidney) was around 87.8 %ID at 24 h p.i., which was 8.4 times higher than that of the 3-nm AuNPs (10.4 %ID). The considerable uptake of non-renal-clearable nanomedicines by these main organs led to short blood circulation time, insufficient tumor targeting, severe body accumulation, and toxicity concerns.

To understand the origin of such difference in the clearance pathways of the 3-nm and 18-nm AuNPs, more fundamental *in vitro* studies were conducted. In addition to the same spherical shape, metal core composition, and identical zwitterionic glutathione coating, similar surface charges were also confirmed with zeta potential measurements. Both the 3-nm and 18-nm AuNPs were negatively charged at physiological pH (7.4) and their zeta potential values were −38.5 ± 1.9 and −42.8 ± 1.9 mV (Fig. 2(e)), respectively. Moreover, the 18-nm AuNPs exhibited strong affinity to serum (fetal bovine serum, FBS) proteins and formed large aggregates (dark blue color inside the rectangle in Fig. 2(f)) from the gel electrophoresis study, which led to rapid uptake by the mononuclear phagocyte system (MPS) and limited circulation time in the body. Similar results were also reported previously: the GS-AuNPs with HD above 6 nm exhibited high affinity to serum proteins, significantly increased overall sizes, and severe accumulation in the major organs [41]. A possible reason is that the particle curvature might change the conformation of glutathione on the particle surface and affect the charge distribution as well as interactions with serum proteins. Meanwhile, the 3-nm AuNPs showed fairly stable properties and were of a desirable size for renal clearance in physiological environments. Therefore, prolonged blood circulation could be achieved with the 3-nm AuNPs as compared with the 18-nm AuNPs. Additionally, we recently reported that ultrasmall metal NPs with higher density (AuNPs) can marginate more rapidly to the blood vessel walls; as a result, in the laminar blood flow, the AuNPs have long blood retention, which allows them to accumulate in tumors more efficiently [42].

2.3 Visualizing the glioma uptake of renal-clearable AuNPs

A unique strength of the 3-nm AuNPs is their near-infrared luminescence with excellent photostability, which allows their accumulation in gliomas to be tracked *in vivo*, *ex vivo*, or with fluorescence microscopy. For advanced intracranial gliomas with large size (>5 mm), selective accumulation of the 3-nm AuNPs in gliomas can be directly seen by invasive *in vivo* imaging at 24 h post-intravenous injection (Fig. 3(a)). With the removal of skin above the mouse skull, the glioma-bearing brain showed intense signal after AuNP injection compared with the control glioma-bearing brain without AuNP administration. It should also be noted that the reason for using light excitation at 470 nm is that the large Stokes shift of these NIR-emitting AuNPs allows us to minimize potential interference from autofluorescence in the tissue background. However, the limited penetration depth of 470 nm is also a major roadblock in their potential applications in clinical settings, which needs to be further addressed in future studies.

Glioma targeting was further confirmed in *ex vivo* imaging (Fig. 3(b)), where the AuNP signal in gliomas increased specifically and significantly. The area in the left hemisphere was identified as a malignant glioma due to abnormal vasculature, as indicated by optical photos in Fig. 3(c). For the control brain without AuNP administration, the tumor area (in the circle) appeared to be slightly darker than the unscathed brain (right hemisphere), which resulted from light absorption by the tumor vasculature.

For less advanced small gliomas (2 to 5 mm) embedded in deep brain locations below the cerebral cortex, little positioning information of these gliomas can be provided by whole-brain *ex vivo* imaging because of the limited tissue penetration depth and autofluorescence interference (Fig. S4 in the ESM). Therefore, horizontal brain tissue sectioning (2 mm in thickness) was performed and fluorescence images were collected as shown in Figs. 3(d) and 3(e). The tumor area was readily recognized from the bright-field images (Fig. 3(e), lower row), which was also confirmed by nuclei staining with Hoechst 33342 (Fig. 4(a)). The fluorescence signal of AuNPs in the tumor area was analyzed and the cortex area was chosen as a control because of its low, stable fluorescence without interference and inconsiderable AuNP accumulation. With the analysis of tumor/cortex (T/C) fluorescence ratio in Fig. 3(f), the AuNP signal in the tumor area increased 4.6 times from 0 (control) to 24 h p.i. This confirmed the features of the 3-nm AuNPs: significant extravasation from blood-tumor barrier into entire tumor and high-specificity targeting.

Fluorescence microscopy imaging provided more information about the extravasation and permeation of AuNPs in the glioma environment. As shown in the images of the tumor/ adjacent brain margin (Fig. 4(a), first row), the cells were readily identified by nuclei staining (Hoechst 33342, colored as blue) and the glioma cells in the tumor area were of distinct density because of their high proliferation rate as compared with cells in the cerebral cortex (Fig. 4(a), second row). In the meantime, the blood vessels were stained with TexasRed-labeled tomato lectin (pseudo green color). The near-infrared signals, recognized as AuNPs, were strong in the glioma area and weak in the cerebral cortex. The merged images showed that the AuNPs mainly accumulated around blood vessels in the gliomas and likely diffused into the tumor interstitium. The AuNP signals disappeared at the distinct margin between the gliomas and the adjacent brain areas. In contrast, the cerebral cortex showed insignificant AuNP signal. To further confirm the observation of AuNP extravasation from glioma blood vessels, we analyzed the signals of AuNPs (NIR) and blood vessels (TexasRed) at the glioma vasculature cross-sections (in terms of full-width half-maximum, FWHM). The ratio of $\mathrm{FWHM}_{\mathrm{AuNPs}}/\mathrm{FWHM}_{\mathrm{Vessels}}$ in the gliomas was 1.80 ± 0.55 while this ratio was 0.91 ± 0.04 in the cortex. This difference further suggested that AuNPs diffused into the glioma interstitial space from vascular structures. This evidence was also consistent with our glioma targeting result of the 3-nm AuNPs without perfusion: As shown in Fig. S5 (in the ESM), 56.2% of the 3-nm AuNPs were found to remain in the gliomas after perfusion. Combining these results, the 3-nm AuNPs can cross the glioma blood vessels and enter its microenvironment, consistent with the high specificity of the 3-nm AuNPs in passively targeting brain tumors.

3 Conclusions

In summary, using a murine glioma model with poor vascular permeability, we investigated passive glioma targeting of renal-clearable AuNPs. As a control, glioma targeting of non-renal-clearable AuNPs was also investigated under the same condition. Our results showed that renal-clearable AuNPs still targeted gliomas with much higher efficiency and specificity through the EPR effect than the non-renal-clearable NPs did, which was mainly due to their long retention time in the blood stream even though they were eventually eliminated through the kidneys rather than through the MPS. In addition, these ultrasmall AuNPs could take advantage of the vascular leakage of gliomas to enter the glioma interstitium and were retained in gliomas for a long period, as indicated by fluorescence co-localization studies of renal-clearable AuNPs and blood vessels and ICP-MS analysis of glioma targeting with or without perfusion. As a result, high-contrast fluorescence imaging of gliomas was achieved. These results suggest that renal-clearable AuNPs with high glioma targeting specificity and high contrast as well as low non-specific accumulation may serve as a new-generation contrast agent for early brain tumor detection once they are integrated with nuclear imaging techniques used in the clinics [43] and their toxicology in large animals is fully unraveled. In addition, it will be also interesting and very important to further understand whether the heterogeneity of blood-tumor barrier properties in different subtypes of gliomas induces different NP accumulation *in vivo* and whether it can facilitate drug delivery to gliomas since the blood vasculature shows heterogeneity in different gliomas (astrocytomas, oligodendrogliomas, etc.) [44] as well as different locations of tumors (from tumor core to invasive peripheral regions) [45, 46].

4 Experimental

4.1 Preparation and characterization of AuNPs with different sizes

The renal-clearable glutathione-coated AuNPs were synthesized according to a reported method [36]. Briefly, a solution containing $HAuCl_4$ (3 mM) and glutathione (2.4 mM) was heated at 95 °C with vigorous stirring for 35 min. With centrifugation at 21,000*g* for 3 min, the supernatant with NPs was collected. The NPs were precipitated with the addition of ethanol in the solution for further purification. The AuNPs suspended in phosphate buffered saline (PBS) were purified with size-exclusion column (Sephadex) and stored in the fridge before further study.

The non-renal-clearable AuNPs were synthesized by solid-state thermal reduction of gold salt [39] and surface replacement. Firstly, 1.8 mL of aqueous solution containing 250 mg of glycine and 13 mg of potassium gold chloride was evaporated and then the mixture in solid phase was thermally reduced at 195 °C and redispersed with 1 mL of deionized water. The suspension was collected by centrifuging at 4,000*g* for 2 min to remove any large aggregates. The AuNPs in the suspension were then precipitated by centrifuging at 7,000*g* to remove small NPs, free ions, and glycine. The purified glycine-stabilized AuNPs were washed twice and dispersed in sodium borate buffer. By the neutralization of solution and addition of 10 mM glutathione with stirring for 15 min, the AuNPs with replaced surface were purified further with a centrifugal filter (molecular-weight cut-off of 50 kDa). The AuNPs were dispersed in PBS for further study.

The size distributions of AuNPs were analyzed by high-resolution transmission electron microscopy (JEOL 2100, 200 kV). The HD of the NPs was obtained with a Brookhaven 90Plus Dynamic Light Scattering Particle Size Analyzer. The absorption spectra were collected using a Varian 50 Bio UV-Vis spectrophotometer. The excitation and emission spectra of the luminescent AuNPs (3 nm) were acquired using a PTI QuantaMaster™ 30 Fluorescence Spectrophotometer (Birmingham, NJ). Zeta potential values of the NPs were analyzed with Brookhaven ZetaPALS zeta potential analyzer.

4.2 Construction of murine glioma model

The animal studies were approved by the institutional animal care and use committee at the UT Southwestern Medical Center and UT Dallas. The nude mice (nu/nu, wt: pink/black, ~20 g, 6–8 weeks old) and balb/c mice were housed in ventilated cages under standard conditions. The 73c glioma cell line was cultured in Dulbecco’s modified Eagle medium (DMEM) with the addition of 10% (v/v) FBS and 1% (v/v) penicillin-streptomycin at 37 °C. To implant the tumor, a suspension containing ~10^4 cells in 2 μL of DMEM (with 10% FBS) was injected into the left hemispheres of the mice. The gliomas were allowed to grow for two weeks and the body weight and mobility of the mice were monitored during the glioma growth.

4.3 Glioma targeting, pharmacokinetics, biodistribution, and renal clearance study

AuNPs with different sizes in 200 μL of PBS were injected into glioma-bearing nude mice ($n = 3$, Foxn1^{nu}) via the tail vein. The gliomas, normal brain tissues, and other organs and tissues were collected, weighed, and dissolved in aqua regia. Gold concentrations in organs and tissues were measured by ICP-MS. The urine was also gathered within 24 h, dissolved in aqua regia, and analyzed by ICP-MS. Pharmacokinetics study was conducted with balb/c mice and blood samples were collected at different post-injection time points and analyzed by ICP-MS.

The *in vitro* serum binding of the 3-nm AuNPs and 18-nm AuNPs was performed by incubation of (1) 3-nm AuNPs, (2) 3-nm AuNPs + 10% (v/v) FBS/CBB, (3) 18-nm AuNPs, (4) 18-nm AuNPs + 10% (v/v) FBS/CBB, and (5) FBS/CBB in PBS at 37 °C for 1 h followed by agarose gel electrophoresis analysis for 30 min.

4.4 Invasive *in vivo* and *ex vivo* imaging

The invasive *in vivo* imaging of mice (at 0 or 24 h p.i.) and *ex vivo* imaging of whole brain and brain slices (at 24 h p.i.) were performed using the Carestream Molecular imaging system *In-Vivo* FX PRO (US) (ex: 470/10 nm; em: 830/20 nm; exposure time: 2 min). The invasive *in vivo* imaging was conducted by removal of skin above the mouse skull; the *ex vivo* imaging was performed with the whole glioma-bearing brains and cross-sectional brain tissues (2 mm in thickness) sliced with mouse brain matrix.

4.5 Fluorescence microscopy imaging

The fluorescence microscopy imaging was performed using an IX-71 inverted microscope (Olympus) with a 40× objective lens and a Photon Max 512 CCD camera (Princeton Instruments). The excitation filter, emission filter, and exposure time for acquiring the fluorescence images were as follows: Hoechst 33342, ex: 350/50 nm and em: 500/2 nm, 100 ms; TexasRed, ex: 560/50 nm and em: 645/75 nm, 100 ms; NIR-emitting AuNPs, ex: 420/40 nm and em: 780(LP) nm, 500 ms.

The brain slices with gliomas were collected at 24 h p.i. and fixed in 4% paraformaldehyde in PBS. The tissues were sliced into sections that were 80 μm in thickness using a vibrating microtome (Leica, VT1000S) and further stained with Hoechst 33342 and TexasRed-labeled tomato lectin. The stained tissues were mounted on microscopy slices before analysis by fluorescence microscopy.

Supplementary Material

Refer to Web version on PubMed Central for supplementary material.

Acknowledgments

This study was partially supported by CPRIT (Nos. RP140544 and RP160866), NIH (No. 1R01DK103363) and a start-up fund from the University of Texas at Dallas to J. Z., UTSW CRI start-up funds, UTSW High Impact/High Risk Grant and NINDS K99/R00 (No. R00NS073735) to W. P. G.

References

1. Matsumura Y, Maeda H. A new concept for macromolecular therapeutics in cancer chemotherapy: Mechanism of tumoritropic accumulation of proteins and the antitumor agent smancs. Cancer Res. 1986; 46:6387–6392. [PubMed: 2946403]
2. Prabhakar U, Maeda H, Jain RK, Sevick-Muraca EM, Zamboni W, Farokhzad OC, Barry ST, Gabizon A, Grodzinski P, Blakey DC. Challenges and key considerations of the enhanced permeability and retention effect for nanomedicine drug delivery in oncology. Cancer Res. 2013; 73:2412–2417. [PubMed: 23423979]
3. Allen TM, Cullis PR. Drug delivery systems: Entering the mainstream. Science. 2004; 303:1818–1822. [PubMed: 15031496]
4. Jain RK, Stylianopoulos T. Delivering nanomedicine to solid tumors. Nat Rev Clin Oncol. 2010; 7:653–664. [PubMed: 20838415]
5. Goldmann E. The growth of malignant disease in man and the lower animals: With special reference to the vascular system. Lancet. 1907; 170:1236–1240.
6. Folkman J. Tumor angiogenesis: Therapeutic implications. N Engl J Med. 1971; 285:1182–1186. [PubMed: 4938153]
7. Dvorak HF, Brown LF, Detmar M, Dvorak AM. Vascular permeability factor/vascular endothelial growth factor, microvascular hyperpermeability, and angiogenesis. Am J Pathol. 1995; 146:1029–1039. [PubMed: 7538264]
8. Carmeliet P, Jain RK. Angiogenesis in cancer and other diseases. Nature. 2000; 407:249–257. [PubMed: 11001068]
9. Iyer AK, Khaled G, Fang J, Maeda H. Exploiting the enhanced permeability and retention effect for tumor targeting. Drug Discov Today. 2006; 11:812–818. [PubMed: 16935749]
10. Hobbs SK, Monsky WL, Yuan F, Roberts WG, Griffith L, Torchilin VP, Jain RK. Regulation of transport pathways in tumor vessels: Role of tumor type and microenvironment. Proc Natl Acad Sci USA. 1998; 95:4607–4612. [PubMed: 9539785]
11. Groothuis DR. The blood-brain and blood-tumor barriers: A review of strategies for increasing drug delivery. Neuro Oncol. 2000; 2:45–59. [PubMed: 11302254]
12. Pardridge WM. The blood-brain barrier: Bottleneck in brain drug development. NeuroRX. 2005; 2:3–14. [PubMed: 15717053]
13. Béduneau A, Saulnier P, Benoit J-P. Active targeting of brain tumors using nanocarriers. Biomaterials. 2007; 28:4947–4967. [PubMed: 17716726]
14. Yan H, Wang L, Wang J, Weng X, Lei H, Wang X, Jiang L, Zhu J, Lu W, Wei X, et al. Two-order targeted brain tumor imaging by using an optical/paramagnetic nanoprobe across the blood brain barrier. ACS Nano. 2012; 6:410–420. [PubMed: 22148835]
15. Cole AJ, David AE, Wang JX, Galbán CJ, Yang VC. Magnetic brain tumor targeting and biodistribution of long-circulating peg-modified, cross-linked starch-coated iron oxide nanoparticles. Biomaterials. 2011; 32:6291–6301. [PubMed: 21684593]
16. Wilhelm S, Tavares AJ, Dai Q, Ohta S, Audet J, Dvorak HF, Chan WC. Analysis of nanoparticle delivery to tumours. Nat Rev Mater. 2016; 1:16014.
17. Chauhan RP, Mathur R, Singh G, Bag N, Singh S, Chuttani K, Kumar BSH, Agrawal SK, Mishra AK. Evaluation of biotinylated magnetic nanoparticles for tumour imaging. J Mater Sci. 2013; 48:3913–3925.
18. Yang XQ, Hong H, Grailer JJ, Rowland IJ, Javadi A, Hurley SA, Xiao YL, Yang Y, Zhang Y, Nickles RJ. cRGD-functionalized, DOX-conjugated, and ^{64}Cu-labeled superparamagnetic iron oxide nanoparticles for targeted anticancer drug delivery and PET/MR imaging. Biomaterials. 2011; 32:4151–4160. [PubMed: 21367450]

19. Meyers JD, Cheng Y, Broome AM, Agnes RS, Schluchter MD, Margevicius S, Wang XN, Kenney ME, Burda C, Basilion JP. Peptide-targeted gold nanoparticles for photodynamic therapy of brain cancer. Part Part Syst Charact. 2015; 32:448–457. [PubMed: 25999665]
20. Hu H, Huang P, Weiss OJ, Yan XF, Yue XY, Zhang MG, Tang YX, Nie LM, Ma Y, Niu G. PET and NIR optical imaging using self-illuminating ^{64}Cu-doped chelator-free gold nanoclusters. Biomaterials. 2014; 35:9868–9876. [PubMed: 25224367]
21. Goel S, Chen F, Hong H, Valdovinos HF, Hernandez R, Shi SX, Barnhart TE, Cai WB. VEGF$_{121}$-conjugated mesoporous silica nanoparticle: A tumor targeted drug delivery system. ACS Appl Mater Interfaces. 2014; 6:21677–21685. [PubMed: 25353068]
22. Chakravarty R, Goel S, Hong H, Chen F, Valdovinos HF, Hernandez R, Barnhart TE, Cai WB. Hollow mesoporous silica nanoparticles for tumor vasculature targeting and pet image-guided drug delivery. Nanomedicine. 2015; 10:1233–1246. [PubMed: 25955122]
23. Chen K, Li Z-B, Wang H, Cai WB, Chen XY. Dual-modality optical and positron emission tomography imaging of vascular endothelial growth factor receptor on tumor vasculature using quantum dots. Eur J Nucl Med Mol Imaging. 2008; 35:2235–2244. [PubMed: 18566815]
24. Cai WB, Chen K, Li Z-B, Gambhir SS, Chen XY. Dual-function probe for PET and near-infrared fluorescence imaging of tumor vasculature. J Nucl Med. 2007; 48:1862–1870. [PubMed: 17942800]
25. Hong GS, Robinson JT, Zhang YJ, Diao S, Antaris AL, Wang QB, Dai HJ. *In vivo* fluorescence imaging with Ag_2S quantum dots in the second near-infrared region. Angew Chem. 2012; 124:9956–9959.
26. Perrault SD, Walkey C, Jennings T, Fischer HC, Chan WCW. Mediating tumor targeting efficiency of nanoparticles through design. Nano Lett. 2009; 9:1909–1915. [PubMed: 19344179]
27. Gao J, Chen K, Luong R, Bouley DM, Mao H, Qiao T, Gambhir SS, Cheng Z. A novel clinically translatable fluorescent nanoparticle for targeted molecular imaging of tumors in living subjects. Nano Lett. 2011; 12:281–286. [PubMed: 22172022]
28. Wang YC, Liu YJ, Luehmann H, Xia XH, Wan DH, Cutler C, Xia YN. Radioluminescent gold nanocages with controlled radioactivity for real-time *in vivo* imaging. Nano Lett. 2013; 13:581–585. [PubMed: 23360442]
29. Son YJ, Jang J-S, Cho YW, Chung H, Park R-W, Kwon IC, Kim I-S, Park JY, Seo SB, Park CR, et al. Biodistribution and anti-tumor efficacy of doxorubicin loaded glycol-chitosan nanoaggregates by EPR effect. J Control Release. 2003; 91:135–145. [PubMed: 12932645]
30. Noguchi Y, Wu J, Duncan R, Strohalm J, Ulbrich K, Akaike T, Maeda H. Early phase tumor accumulation of macromolecules: A great difference in clearance rate between tumor and normal tissues. Jpn J Cancer Res. 1998; 89:307–314. [PubMed: 9600125]
31. Yu MX, Zheng J. Clearance pathways and tumor targeting of imaging nanoparticles. ACS Nano. 2015; 9:6655–6674. [PubMed: 26149184]
32. Storm G, Belliot SO, Daemen T, Lasic DD. Surface modification of nanoparticles to oppose uptake by the mononuclear phagocyte system. Adv Drug Del Rev. 1995; 17:31–48.
33. Gibaud S, Demoy M, Andreux JP, Weingarten C, Gouritin B, Couvreur P. Cells involved in the capture of nanoparticles in hematopoietic organs. J Pharm Sci. 1996; 85:944–950. [PubMed: 8877884]
34. Brigger I, Dubernet C, Couvreur P. Nanoparticles in cancer therapy and diagnosis. Adv Drug Del Rev. 2002; 54:631–651.
35. De Jong WH, Borm PJA. Drug delivery and nanoparticles: Applications and hazards. Int J Nanomedicine. 2008; 3:133–149. [PubMed: 18686775]
36. Liu JB, Yu MX, Zhou C, Yang SY, Ning XH, Zheng J. Passive tumor targeting of renal-clearable luminescent gold nanoparticles: Long tumor retention and fast normal tissue clearance. J Am Chem Soc. 2013; 135:4978–4981. [PubMed: 23506476]
37. Liu JB, Yu MX, Ning XH, Zhou C, Yang SY, Zheng J. PEGylation and zwitterionization: Pros and cons in the renal clearance and tumor targeting of near-IR-emitting gold nanoparticles. Angew Chem Int Ed. 2013; 52:12572–12576.
38. Black KL, Ningaraj NS. Modulation of brain tumor capillaries for enhanced drug delivery selectively to brain tumor. Cancer Control. 2004; 11:165–173. [PubMed: 15153840]

39. Zheng J, Ding Y, Tian BZ, Wang ZL, Zhuang XW. Luminescent and raman active silver nanoparticles with polycrystalline structure. J Am Chem Soc. 2008; 130:10472–10473. [PubMed: 18636722]

40. Mashimo T, Pichumani K, Vemireddy V, Hatanpaa KJ, Singh DK, Sirasanagandla S, Nannepaga S, Piccirillo SG, Kovacs Z, Foong C, et al. Acetate is a bioenergetic substrate for human glioblastoma and brain metastases. Cell. 2014; 159:1603–1614. [PubMed: 25525878]

41. Zhou C, Long M, Qin YP, Sun XK, Zheng J. Luminescent gold nanoparticles with efficient renal clearance. Angew Chem Int Ed. 2011; 50:3168–3172.

42. Tang SH, Peng CQ, Xu J, Du BJ, Wang QX, Vinluan RD III, Yu MX, Kim MJ, Zheng J. Tailoring renal clearance and tumor targeting of ultrasmall metal nanoparticles with particle density. Angew Chem Int Ed. 2016; 55:16039–16043.

43. Zhou C, Hao GY, Thomas P, Liu JB, Yu MX, Sun SS, Öz OK, Sun XK, Zheng J. Near-infrared emitting radioactive gold nanoparticles with molecular pharmacokinetics. Angew Chem. 2012; 124:10265–10269.

44. Zhu Y, Parada LF. The molecular and genetic basis of neurological tumours. Nat Rev Cancer. 2002; 2:616–626. [PubMed: 12154354]

45. Van Tellingen O, Yetkin-Arik B, de Gooijer MC, Wesseling P, Wurdinger T, de Vries HE. Overcoming the blood-brain tumor barrier for effective glioblastoma treatment. Drug Resist Updat. 2015; 19:1–12. [PubMed: 25791797]

46. Leten C, Struys T, Dresselaers T, Himmelreich U. *In vivo* and *ex vivo* assessment of the blood brain barrier integrity in different glioblastoma animal models. J Neurooncol. 2014; 119:297–306. [PubMed: 24990826]

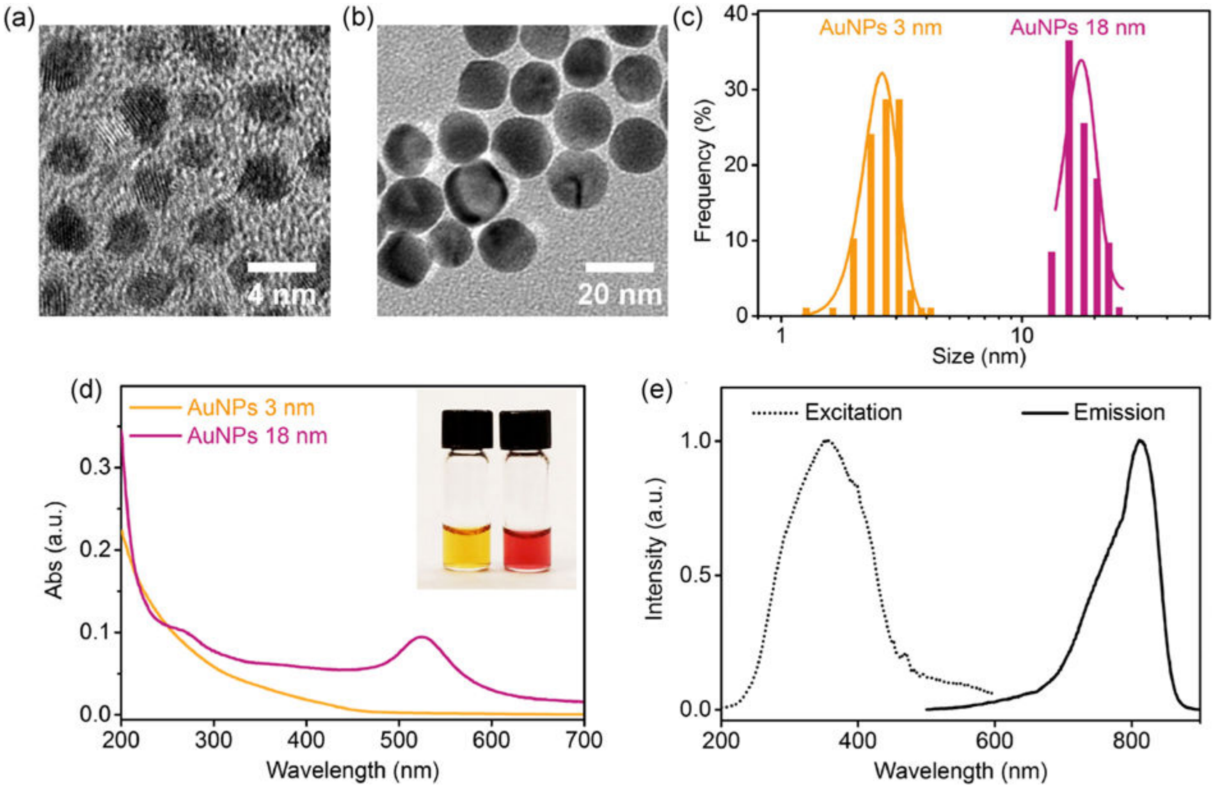

Figure 1.

(a) and (b) Transmission electron microscopy images and (c) size analysis of renal-clearable and non-renal-clearable glutathione-coated AuNPs, showing core sizes of 2.6 ± 0.4 and 17.4 ± 2.4 nm, respectively. (d) Absorption spectra of AuNPs of 3 and 18 nm. Inset: AuNPs of 3 and 18 nm in aqueous solution, from left to right. (e) Excitation and emission spectra of 3-nm AuNPs.

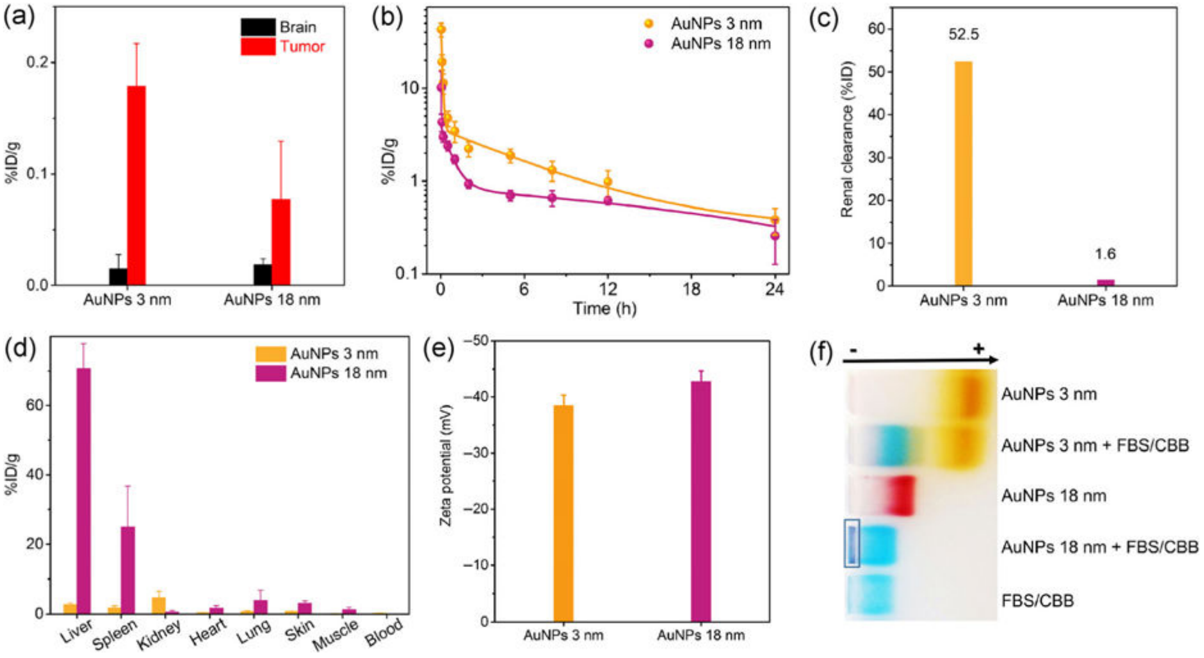

Figure 2.

(a) Distribution of AuNPs with different sizes in gliomas and normal brain tissues at 24 h p.i. (*n* = 3). Before collecting the organs, AuNPs in the bloodstream were removed by perfusion. (b) Pharmacokinetics, (c) renal clearance efficiency, and (d) biodistribution of AuNPs with different sizes at 24 h p.i. (*n* = 3). (e) Zeta potential values of 3-nm and 18-nm AuNPs in PBS at pH 7.4. (f) Serum binding test of 3-nm AuNPs and 18-nm AuNPs by gel electrophoresis. The dark blue color in the rectangle was derived from serum binding and aggregation of 18-nm AuNPs. CBB, Coomassie brilliant blue dye was added to stain FBS. AuNPs were incubated with 10% (v/v) FBS in PBS at 37 °C for 1 h.

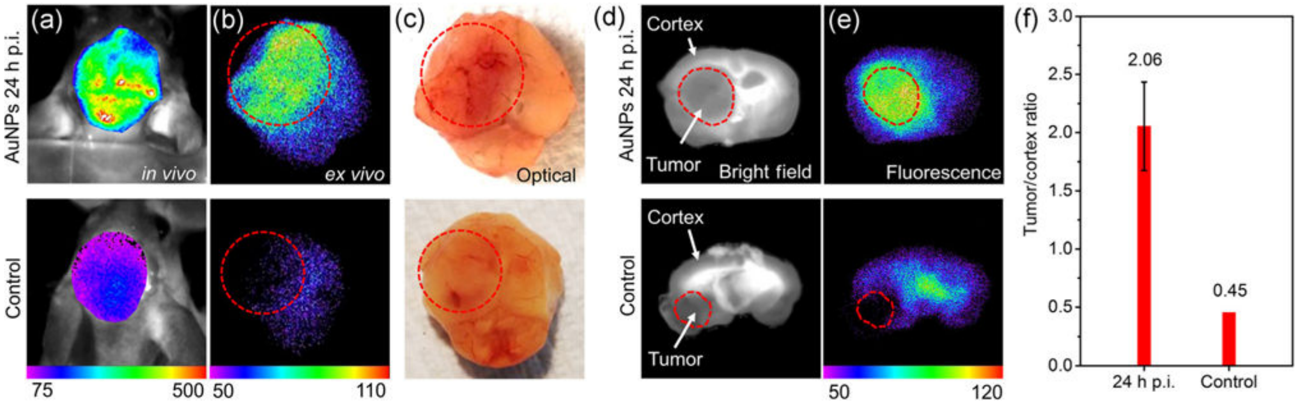

Figure 3.

(a) Invasive *in vivo*, (b) *ex vivo* fluorescence imaging, and (c) optical imaging of advanced glioma-bearing brain with (upper row, 24 h p.i.) or without (lower row) administration of 3-nm AuNPs. (d) Bright-field and (e) fluorescence imaging of less advanced glioma-bearing brain slices with (upper row, 24 h p.i.) or without (lower row) administration of 3-nm AuNPs. (f) Tumor/cortex fluorescence ratio at different time points, which showed a significant increase in tumor/cortex ratio (4.6 times) from control to 24 h p.i.

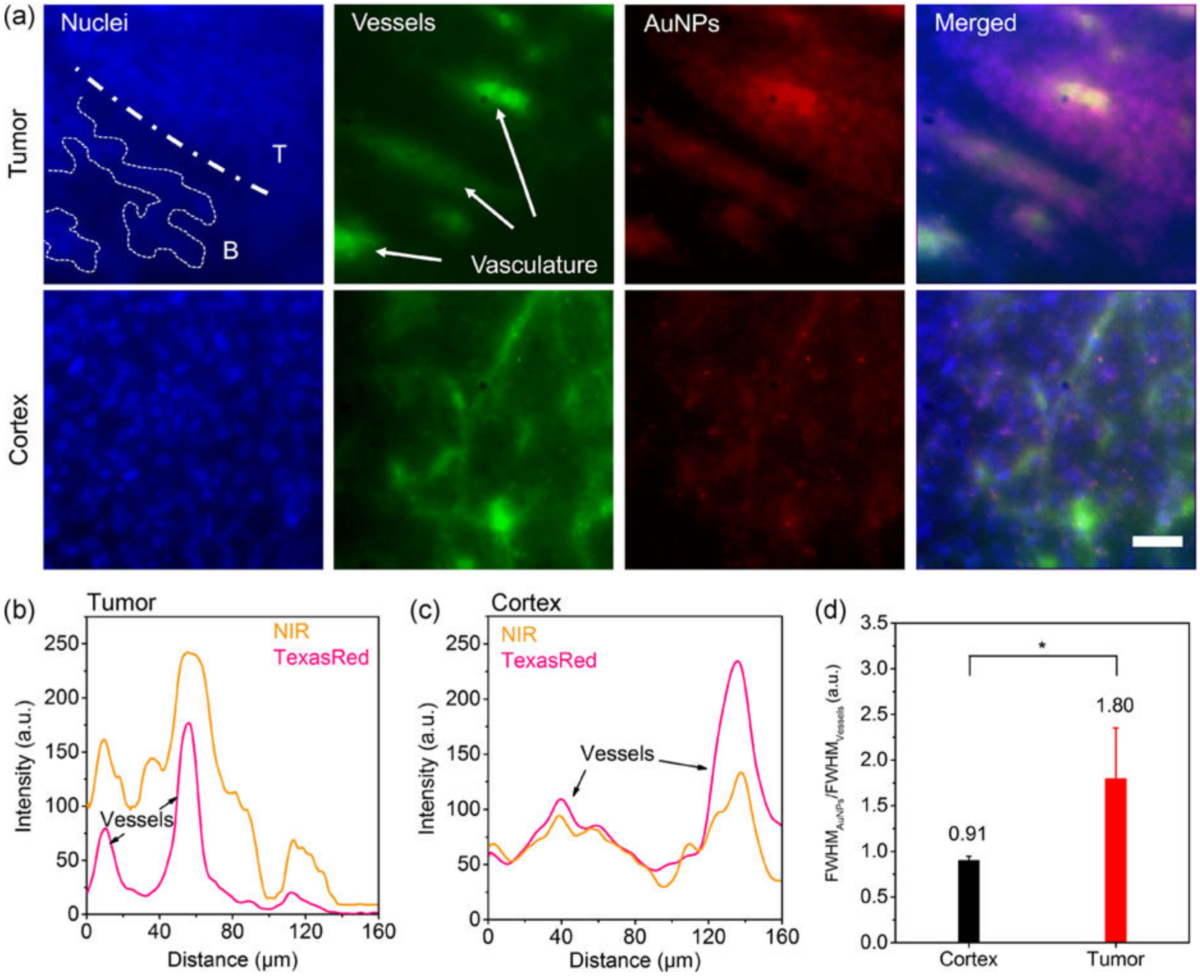

Figure 4.

(a) Fluorescence microscopy images of cortical region and glioma area with 3-nm AuNPs 24 h p.i. (40×, scale bar: 30 μm). The tumor/brain margin is labeled as dot-dash line (T, tumor; B, adjacent brain region without gliomas), and the migration of glioma cells into the neighboring brain tissues is marked. The vasculature in gliomas is pointed out with arrows. Nuclei, Hoechst 33342. (b) and (c) Fluorescence intensities of NIR (near-infrared-emitting AuNPs) and TexasRed (blood vessels, stained by TexasRed tomato lectin) in tumor and cortex cross-sections. AuNP signal showed diffusion pattern in the co-localization of the NPs and tumor vessels, whereas weak AuNP signal was detected in the cerebral cortex. (d) FWHM ratio (AuNPs/vessels) in the tumor and cerebral cortex unveiled the extravasation and permeation of AuNPs in the tumor environment. (*$P < 0.05$, two-tailed Student's *t*-test)